



Title	Simultaneous analysis of slope instabilities on a small catchment-scale using coupled surface and subsurface flows
Author(s)	Zhu, Yulong; Ishikawa, Tatsuya; Subramanian, Srikrishnan Siva; Luo, Bin
Citation	Engineering geology, 275, 105750 https://doi.org/10.1016/j.enggeo.2020.105750
Issue Date	2020-09-20
Doc URL	http://hdl.handle.net/2115/86199
Rights	© <2020>. This manuscript version is made available under the CC-BY-NC-ND 4.0 license http://creativecommons.org/licenses/by-nc-nd/4.0/
Rights(URL)	http://creativecommons.org/licenses/by-nc-nd/4.0/
Type	article (author version)
File Information	Simultaneous Analysis of Slope Instabilities on a Small Catchment-scale using Coupled Surface and Subsurface Flows.pdf



[Instructions for use](#)

1 **Simultaneous Analysis of Slope Instabilities on a Small Catchment-scale using Coupled Surface**
2 **and Subsurface Flows**

3 **Yulong Zhu^a, Tatsuya Ishikawa^{b*}, Srikrishnan Siva Subramanian^c, and Bin Luo^d**

4 ^{a)} Yulong Zhu

5 Laboratory of Analytical Geomechanics, Graduate School of Engineering, Hokkaido University, Japan

6 e-mail: zhuyulong@eis.hokudai.ac.jp

7 ^{b*)} Tatsuya Ishikawa (**Corresponding author**)

8 Faculty of Engineering, Hokkaido University, Kita 13, Nishi 8, Kita-ku, Sapporo, Hokkaido 060-8628, Japan

9 e-mail: t-ishika@eng.hokudai.ac.jp

10 ^{c)} Srikrishnan Siva Subramanian

11 State Key Laboratory of Geohazard Prevention and Geo-environment Protection, Chengdu University of

12 Technology, China

13 e-mail: srikrishnan@frontier.hokudai.ac.jp

14 ^{d)} Bin Luo

15 Department of Road and Bridge Engineering, School of Civil Engineering, Sichuan Agricultural University,

16 China

17 e-mail: bin-luo@sicau.edu.cn

18

19

20

21

22

23

24

25

26

27

Highlights

28

29 1. A coupled model of surface flow, subsurface flow, and soil mechanics is proposed.

30 2. Slope instabilities are analyzed on a small catchment-scale.

31 3. Runoff increases the possibility of embankment collapse at the exit of the gully.

32

33 **Abstract**

34 High-velocity runoff generated in hillslopes during heavy rainfall caused by typhoon increases
35 the instability of the embankment slope at the exit of the gully. Such effects of high-velocity
36 runoff are usually neglected in conventional rainfall-induced slope failure analysis. In order to
37 consider the effects of runoff on the slope instability, this study attempts to simulate the runoff,
38 infiltration, seepage, and slope instabilities on a small catchment-scale simultaneously. For this
39 purpose, this study firstly proposes a coupled model of surface flow, subsurface flow, and soil
40 mechanics based on shallow water equations, Richards's equation, Green-Ampt infiltration
41 capacity model, and local factor of safety (LFS) approach. Next, to make the proposed coupled
42 model effective in the practical analysis of runoff, a diffusion wave approximation of shallow
43 water equations is validated by numerical simulations, and then it is used to replace shallow
44 water equations in the proposed coupled model. Finally, the proposed coupled model is verified
45 by Abdul and Gillham system and applied to a natural slope in Hokkaido, Japan. The numerical
46 results highlight the influences of runoff from upstream on the embankment slope failure at the
47 exit of the gully. Furthermore, the small catchment-scale slope instabilities assessment
48 approach proposed in this study provides an effective approach for simulating heavy rainfall
49 induced runoff and slope instabilities. The distribution map of the factor of safety (FOS) has
50 significant implications for precisely determining the dangerous spots (instead of areas) on a
51 small catchment-scale and accurately releasing the warning information to these dangerous
52 spots.

53 **Keywords:** Surface flow; Subsurface flow; Slope instabilities; Local factor of safety

54 **1 Introduction**

55 The rainstorms and unexpected typhoons cause sediment-related disasters threatening
56 the lives and public property in many parts of the world, especially in rainy mountainous

57 terrains. During a rainstorm, the infiltration capacity of the slope is not enough to absorb all
58 the rainwater into the soil, resulting in the rainwater that cannot infiltrate into the soil flows in
59 the form of runoff on the slope surface (Cuomo and Della Sala, 2013; Kean et al., 2013; Wei
60 et al., 2017; Van Asch et al., 2018). Both rainwater infiltration and runoff could deteriorate the
61 slope stability. The rainwater infiltration causes a decrease in the suction in the unsaturated
62 zone and an increase in positive pore pressure in the saturated zone due to groundwater, which
63 eventually induces the occurrence of landslide/slope failure (Chowdhury and Flentje, 2002;
64 Rahardjo et al., 2005; Acharya et al., 2009; Zhang et al., 2014). On the other hand, the runoff,
65 i.e. fast-flowing surface water, may cause erosion of the slope surface or pond in the concave
66 areas increasing the possibility of slope failure at some locations such as a road embankment
67 which crosses a gully. For example, during the summer season (August-September), the
68 Japanese archipelago is often struck by violent typhoons with extremely intense rainfalls,
69 which cause a large number of disasters, e.g. floods, debris flows, and landslides (Wang and
70 Sassa, 2003; Fujisawa et al., 2010). According to the statistics of the Ministry of Land,
71 Infrastructure, Transport, and Tourism (MLIT), there are 200,000 dangerous valleys and slopes
72 in Japan, and about 1,000 landslide disasters reported annually (Osanai et al., 2010).

73 Both on catchment-scale and slope-scale, when analyzing the unsaturated soil slope
74 instability under rainwater infiltration, for simplification, the influences of runoff are usually
75 neglected (Liu et al., 2017; Chiu et al., 2019). In this case, two assumptions of the rainfall
76 infiltration are generally used. One is that the rainfall infiltration is equal to the rainfall intensity.
77 Another is that rainfall infiltration is equal to the component of rainfall intensity perpendicular
78 to the boundary. Obviously, the above assumptions cannot fully reproduce the actual processes
79 of rainfall/runoff infiltration, especially under heavy rainfall conditions (rainfall intensity is
80 much larger than the infiltration capacity). Therefore, earlier studies made many attempts to

81 develop models that can describe the behavior of surface and subsurface flows. [Tian and Liu](#)
82 [\(2011\)](#) coupled two-dimensional (2D) Saint Venant equations and three-dimensional (3D)
83 Richards's equation in an Integrated Surface Water-Ground water Model (ISWGM).
84 [Fernández-Pato et al. \(2016\)](#) combined 2D shallow water equations with two infiltration
85 models, Horton model and Green-Ampt model, for estimating the runoff and infiltration in a
86 watershed. However, there are no simplified methods or numerical models developed to
87 simulate the slope instability by coupled surface and subsurface flows during heavy rainfall.

88 From the view of slope stability analysis, the limit-equilibrium method (LEM) and
89 shear strength reduction technique (SSRT) are commonly used in some general commercial
90 software packages e.g. GeoStudio ([GEO-SLOPE International, 2007](#)) and FLAC^{3D} ([Itasca,](#)
91 [2012](#)). The LEM discretizes the mass of a potential failure slope into smaller vertical slices and
92 assesses the ratio of shear strength to shear stress for all slices as the factor of safety (FOS) of
93 an identified or assumed potential failure surface ([Bishop, 1955](#); [Morgenstern and Price, 1965](#)).
94 While the determination of where the failure initiates or the ultimate geometry and position of
95 a landslide failure surface is one of the fundamental challenges when using LEM ([Lu et al.,](#)
96 [2012](#)). Unlike conventional LEM, it is not necessary to specify the shape of the failure surface
97 in advance when using the SSRT ([Sciarra et al., 2017](#); [Pasculli et al., 2018](#)). The FOS is defined
98 as the ratio of the real shear strength to the reduced shear strength of the soil. The failure surface
99 is determined by reducing the shear strength parameters (cohesion and friction angle) of the
100 soil until the slope becomes unstable ([Farshidfar and Nayeri, 2015](#)). However, it is worth noting
101 that LEM and SSRT are effective for the stability analysis of a single slope but not feasible for
102 the analysis of slope instabilities on a catchment-scale. [Lu et al. \(2012\)](#) proposed an approach,
103 i.e. local factor of safety (LFS) approach to quantify the FOS of a slope under rainwater
104 infiltration, and verified that the assessment of the LFS approach is consistent with the LEM.

105 Furthermore, the LFS approach has the potential to overcome several major limitations in the
106 classical FOS methodologies, such as the initiation and evolution of instability with changes in
107 pore water pressure, and the inherent underestimation of slope instability (Lu et al., 2012).
108 Besides, when analyzing the stability of multi slopes (more than one slope), LEM and SSRT
109 need to analyze the slopes one by one. However, the LFS approach also has the potential to
110 give the distribution map of FOS. Therefore, in this study, the LFS approach is used to assess
111 the slope instabilities on a small catchment-scale.

112 Accordingly, the objectives of this study are to (1) develop a coupled model of surface
113 flow and subsurface flow to simulate the relationship between rainfall, runoff, and infiltration
114 under heavy rainfall conditions; (2) model the rainfall/runoff induced slope instabilities to
115 determine the dangerous spots on a small catchment-scale. For these purposes, this study firstly
116 proposes a coupled model of surface flow, subsurface flow, and soil mechanics to
117 simultaneously simulate runoff, infiltration, seepage, and slope instabilities on a small
118 catchment-scale. Surface flow is governed by 2D shallow water equations. Subsurface flow is
119 governed by 3D Richards's equation. Two well-known models, namely Horton model (Horton,
120 1933) and Green-Ampt model (Green and Ampt, 1911), are commonly used to estimate soil
121 infiltration capacity. The parameters in the Horton model have no clear physical basis and must
122 be estimated from the experimental data, while the parameters in the Green-Ampt model have
123 physical meaning and can be estimated from soil properties (Fernández-Pato et al., 2016).
124 Therefore, the Green-Ampt model is used in this study for estimating the infiltration capacity
125 of the ground surface, which could be used to determine the boundary conditions of subsurface
126 flow analysis. The LFS approach is used to assess the slope instabilities on a small catchment-
127 scale. Next, to make the proposed coupled model effective in the practical analysis of runoff,
128 a diffusion wave approximation of shallow water equations is validated based on numerical

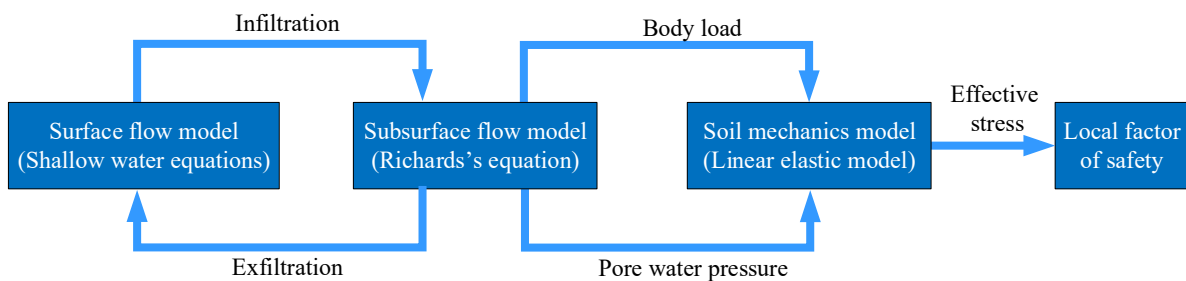
129 simulations. Afterward, the diffusion wave approximation is used to replace shallow water
130 equations in the proposed coupled model. Then, the proposed coupled model is verified by
131 Abdul and Gillham system ([Abdul and Gillham, 1984](#)). Finally, the simulation of surface flow,
132 subsurface flow, and slope instabilities for a natural mountain area in Hokkaido, Japan is
133 performed by using the proposed coupled model.

134 **2 Numerical Modeling Strategy**

135 The surface and subsurface flows are complex environmental systems that often behave
136 in a coupled manner. In this study, a coupled model of surface flow, subsurface flow, and soil
137 mechanics is proposed by using a finite element software, COMSOL Multiphysics ([COMSOL
138 Multiphysics, 2018](#)). In the coupled model, the 3D soil mechanics model (linear elastic model)
139 is established by the solid mechanics module of COMSOL. The 2D surface flow model
140 (shallow water equations) and 3D subsurface flow model (Richards's equations) are established
141 by the PDEs (partial differential equations) module of COMSOL. The surface flow model and
142 subsurface flow model are coupled through infiltration and exfiltration. The subsurface flow
143 model and soil mechanics model are coupled in two ways: (1) the body load function that
144 depends on the volumetric water content is applied to a linear elastic soil mechanics model to
145 manifest the effect of moisture variation on the self-weight and stress distribution, and (2) the
146 effect of volumetric water content variation on the pore water pressure (suction) is considered
147 for evaluating effective stress. Accordingly, the local factor of safety can be calculated by using
148 effective stress as shown in Fig. 1.

149 During torrential rain, rainwater infiltration is a two-stage process, i.e. rainfall
150 infiltration (rainfall derived infiltration) in the early stage of the rainfall event, and runoff
151 infiltration (runoff derived infiltration, in this case, the infiltration is controlled by the pressure
152 gradient rather than the rainfall intensity) in the later stage of the rainfall event. Therefore, the

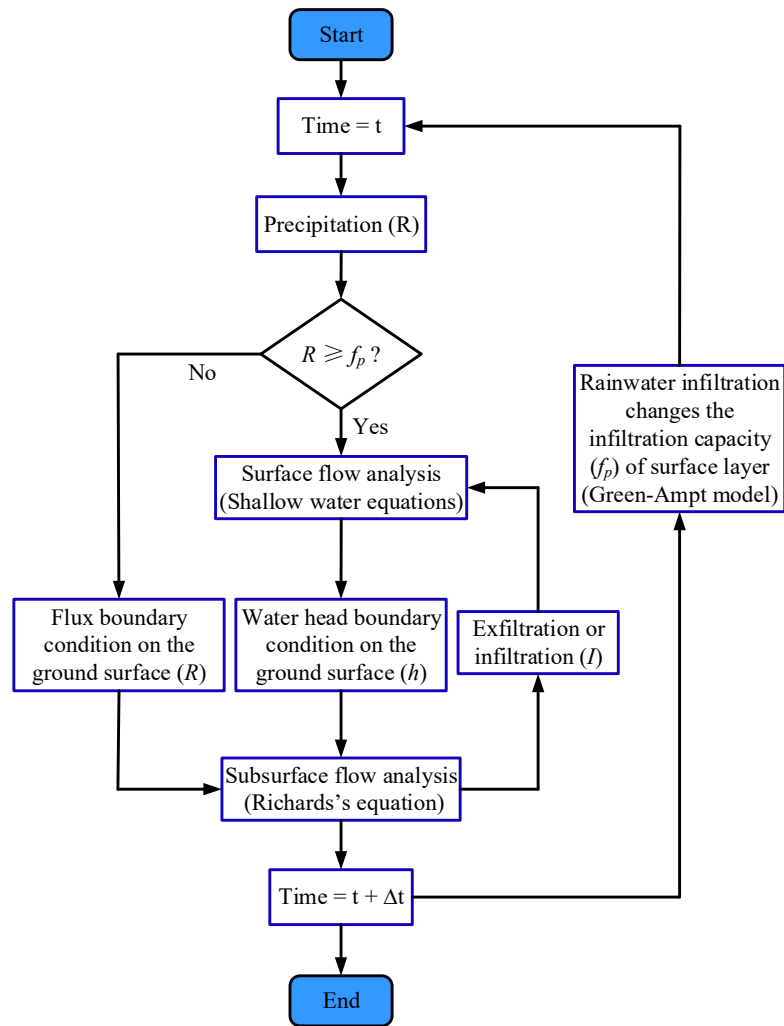
153 Green-Ampt model is used for estimating the infiltration capacity (f_p) of the ground surface to
 154 determine the boundary conditions of subsurface flow analysis. That is in the early stage of the
 155 rainfall event, as the rainfall intensity (R) is usually weak and less than the infiltration capacity
 156 (f_p) of the ground surface, the Richards's equation is directly solved with a flux boundary
 157 condition at the surface. If the rainfall intensity exceeds the infiltration capacity (f_p), part of
 158 rainwater infiltrates into the ground, and the rest generates runoff on the ground surface. On
 159 the other hand, the exfiltration (positive value) and infiltration (negative value) calculated from
 160 the subsurface flow model is added to the surface flow model as a source and sink item. Then,
 161 the infiltrated rainwater causes the decrease of the infiltration capacity (f_p) of the ground surface,
 162 and the calculation of the next timestep will be carried out. This study proposes an iterative
 163 cross-coupled surface and subsurface flows model to simulate this process. The flowchart of
 164 the time-marching scheme in iterative cross-coupled surface and subsurface flows model is
 165 shown in Fig. 2.



166

167

Fig. 1. Scheme of the proposed coupled hydrological and slope stability model.



168

169

Fig. 2. Flowchart of the time-marching scheme in iterative cross-coupled surface and

170

subsurface flows model.

171

3 Governing Equations

172

The governing equations in the proposed coupled model are represented in this part.

173

The surface flow is governed by the 2D shallow water equations, and the subsurface flow is

174

governed by the 3D Richards's equation. The soil infiltration capacity is estimated by the

175

Green-Ampt model, and the slope instabilities are assessed by the LFS approach.

176 3.1 Governing equation for surface flow

177 Surface flow is calculated by 2D shallow water equations which can be expressed as
 178 follows (Murillo et al., 2007).

179 Equation of continuity:

$$180 \quad \frac{\partial h}{\partial t} + \frac{\partial(hu)}{\partial x} + \frac{\partial(hv)}{\partial y} = R - I \quad (1)$$

181 Equations of motion:

$$182 \quad \frac{\partial(uh)}{\partial t} + \frac{\partial(hu^2)}{\partial x} + \frac{\partial(huv)}{\partial y} = -hg \frac{\partial H}{\partial x} - hgS_{fx} + D_x \quad (2)$$

$$183 \quad \frac{\partial(vh)}{\partial t} + \frac{\partial(huv)}{\partial x} + \frac{\partial(hv^2)}{\partial y} = -hg \frac{\partial H}{\partial y} - hgS_{fy} + D_y \quad (3)$$

184 where, h is water depth (m); u , v is water velocity in the x and y direction (m/s); R is rainfall
 185 intensity (m/s); I is infiltration rate (m/s); g is the gravitational acceleration (m/s^2); H is water
 186 surface elevation (m); t is time (s); D_x , D_y is advection term in the x and y direction; S_{fx} , S_{fy} is
 187 the friction slope in the x and y direction respectively, usually written in term of the Manning's
 188 roughness coefficient n_m ($s/m^{1/3}$).

$$189 \quad S_{fx} = n_m^2 u \sqrt{u^2 + v^2} / h^{4/3}, S_{fy} = n_m^2 v \sqrt{u^2 + v^2} / h^{4/3} \quad (4)$$

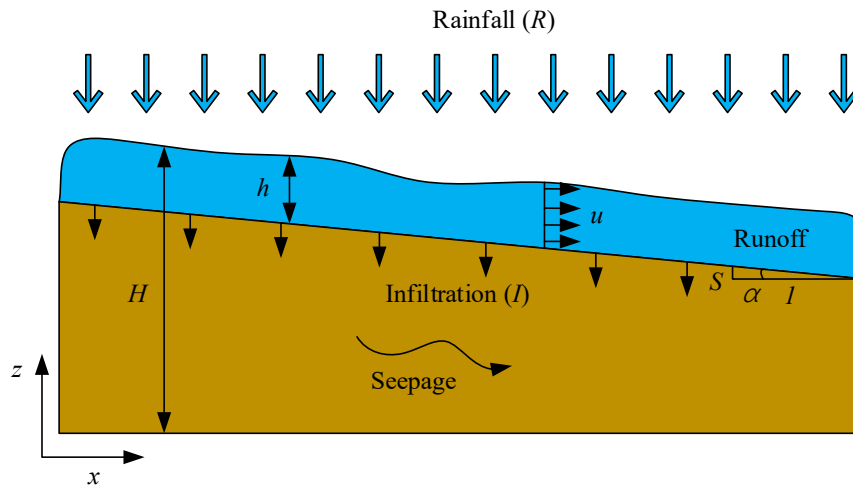
190 The first terms on the right-hand side of the equations of motion, Eq. (2) and Eq. (3),
 191 represent the driving forces from the slope gradient and water depth gradient. The second terms
 192 represent the drag forces due to friction (friction loss gradient). The third terms are advection
 193 terms, and they can be assumed by the following conditions.

$$194 \quad D_x = \frac{\partial}{\partial x} \left[v_t \frac{\partial(uh)}{\partial x} \right] + \frac{\partial}{\partial y} \left[v_t \frac{\partial(uh)}{\partial y} \right], \quad D_y = \frac{\partial}{\partial x} \left[v_t \frac{\partial(vh)}{\partial x} \right] + \frac{\partial}{\partial y} \left[v_t \frac{\partial(vh)}{\partial y} \right] \quad (5)$$

195 In which, v_t is eddy viscosity coefficient (m^2/s), and it can be assumed as follows (Zeng
 196 et al., 2010).

197
$$v_t = \lambda h U^* \text{ and } U^* = \sqrt{ghS} \tag{6}$$

198 where, U^* is the frictional velocity (m/s); λ is dimensionless eddy viscosity, and its standard
 199 value for an infinitely wide channel is 0.067 (Zeng et al., 2010); S is the gradient of water
 200 surface. As the water depth gradient is much smaller than the slope gradient, it can be assumed
 201 that S is equal to the slope gradient (Weill et al., 2009) as shown in Fig. 3.



202

203 **Fig. 3.** Conceptual schematic of the surface flow model.

204 In principle, by simultaneously solving the equations of continuity and motion, the
 205 behavior of the surface runoff can be tracked, and the water depth and velocity can be obtained
 206 at any interesting location. However, the timesteps need to be set very small, or simulations
 207 only can be performed under relatively flat terrain conditions. It causes the low calculation
 208 efficiency of shallow water equations when performing the practical runoff analysis in vast
 209 mountainous areas (Rengers et al., 2016). The main reason can be considered as that some
 210 insignificant terms in the equation of motion, Eq. (2) and Eq. (3), significantly increase the
 211 calculation time and decrease convergence. Therefore, to ignore the insignificant terms in the
 212 equations of motion, the contribution of each term is examined by performing numerical
 213 simulations using seven surface flow models with different slope angles ($<1^\circ$, 5° , 10° , 15° , 30° ,

214 45°, and 60°). In the surface flow model, Manning's coefficient value is 0.3 s/m^{1/3}. A fixed
 215 water head boundary condition ($h=0.001$ m) is applied to the left side and zero gradient
 216 boundary condition ($\partial h/\partial x=0$) is applied on the right side. The simulation time is 10 s with the
 217 timestep of 1.0×10^{-4} s. Table 1 shows the simulation results, i.e. the contribution of each term
 218 in Eq. (2) as a fraction of 100 % of the total for surface water flow under different slope angles.

219 **Table 1** Contribution of each term in the equations of motion for surface water flow.

Slope angle (°)	Inertia term $\frac{\partial(uh)}{\partial t}$ (%)	Velocity term $\frac{\partial(hu^2)}{\partial x}$ (%)	Driving force term $-hg\frac{\partial H}{\partial x}$ (%)	Friction term $-hgS_{fx}$ (%)	Advection term D_x (%)
<1	<0.001	<0.001	50.038	49.961	<0.001
5	<0.001	0.005	49.584	50.410	<0.001
10	<0.001	0.011	49.595	50.393	<0.001
15	0.003	0.015	49.535	50.446	0.001
30	0.024	0.219	52.537	47.200	0.020
45	0.051	0.850	44.260	54.730	0.109
60	0.159	0.327	50.808	48.679	0.027

220 From the results, it is clear that the sum of the driving force term and friction term
 221 accounts for over 99% for all types, while the total contribution of the inertia term, advection
 222 term, and velocity term is less than 1% together. Therefore, the following diffusion wave
 223 approximation can be typically used in practice.

224
$$S_{fx} + \frac{\partial H}{\partial x} = 0 \quad (7)$$

225
$$S_{fy} + \frac{\partial H}{\partial y} = 0 \quad (8)$$

226 After substituting Eq. (4) into Eq. (7) and Eq. (8), the expressions for the components
 227 of the velocity vector can be obtained as follows.

228
$$u = -\frac{h^{2/3}}{n_m\sqrt{|S|}}\nabla_x(H), \quad v = -\frac{h^{2/3}}{n_m\sqrt{|S|}}\nabla_y(H) \quad (9)$$

229 Finally, Eq. (1) can be written as follows, and then it is used to replace shallow water
230 equations in the proposed coupled model.

231
$$\frac{\partial h}{\partial t} - \nabla \left(\frac{h^{5/3}}{n_m\sqrt{|S|}}\nabla(H) \right) = R - I \quad (10)$$

232 3.2 Governing equation for subsurface flow

233 When performing subsurface flow analysis in unsaturated soils, two well-known
234 methods are commonly used: Richards's equations and two-phase Darcy's law method.
235 Compared with the two-phase Darcy's law method, Richards's equation is simple in form and
236 the physical meaning of each parameter is relatively clear. Therefore, the subsurface flow is
237 governed by 3D Richards's equation (Richards, 1931).

238
$$\nabla \cdot [k_s k_r \cdot \nabla(H_p + z)] + Q_w = [C_m + S_e S_c] \frac{\partial H_p}{\partial t} \quad (11)$$

239 where, C_m is specific moisture capacity (m^{-1}); S_c is specific storage coefficient (m^{-1}); S_e is the
240 effective degree of saturation; H_p is pressure head (H_p is negative in unsaturated soil, and
241 positive in saturated soil) (m); z is elevation (m); k_r is relative hydraulic conductivity; k_s is
242 saturated hydraulic conductivity (m/s); Q_w is sink and source of water (s^{-1}).

243 van Genuchten (1980) proposed a Soil Water Characteristic Curve (SWCC) to describe
244 the relationship in C_m , S_e , k_r , θ , and H_p in unsaturated soil. As shown in Eq. (12) to Eq. (15),
245 these parameters could be specified by the saturated and residual volumetric water content θ_s
246 and θ_r , as well as constants of a , n , m , and l .

247
$$\theta = \theta_r + S_e(\theta_s - \theta_r) \quad (12)$$

248
$$S_e = \frac{1}{[1+(aH_p)^n]^m}, \quad m = 1 - \frac{1}{n} \quad (13)$$

249
$$C_m = \frac{am}{1-m} (\theta_s - \theta_r) S_e^{\frac{1}{m}} (1 - S_e^{\frac{1}{m}})^m \quad (14)$$

250
$$k_r = S_e^l \left[1 - (1 - S_e^{\frac{1}{m}})^m \right]^2 \quad (15)$$

251 **3.3 Soil infiltration capacity model**

252 The Green-Ampt model (Green and Ampt, 1911) assumes that the soil infiltration
 253 capacity is governed by the soil properties and rainfall conditions. The soil infiltration capacity,
 254 f_p , can be approximated as follows.

255
$$f_p = k_s \left(1 + \frac{\Psi \Delta \theta}{F} \right) \quad (16)$$

256 where, f_p is infiltration capacity (m/s); ψ is the average suction head at the wetting front (m),
 257 and $\Delta \theta$ is the difference between the saturated volumetric water content, θ_s , and the initial
 258 volumetric water content, θ_i , ($\Delta \theta = \theta_s - \theta_i$) (m^3/m^3). F is the cumulative infiltration (m).

259
$$F = \int_0^t I dt \quad (17)$$

260 In this study, it is considered that the Green-Ampt model is only used to estimate the
 261 infiltration capacity (f_p) during the rainfall infiltration stage and determine when the runoff
 262 generate. At the beginning of the simulation, a profile with initial moisture content is used to
 263 determine the initial infiltration capacity of the ground surface. With infiltration of the
 264 rainwater, the Green-Ampt model is running and infiltration capacity will be redistributed at
 265 each timestep according to Eq. 16. Afterward, the rainfall intensity at the next timestep will be
 266 compared with the updated infiltration capacity. If the rainfall intensity exceeds the infiltration
 267 capacity of the ground surface, the water is ponding on the ground surface. The infiltration rate
 268 will be determined by pressure head at the surface (zero or higher depending on the increasing
 269 runoff h) and the pressure head in the cell below. A part of the not infiltrated water and the
 270 exfiltrated water from the underground will then be applied to the runoff simulation as source
 271 item in the next timestep.

272 3.4 3D soil mechanics model (LFS approach)

273 [Lu et al. \(2012\)](#) proposed the LFS approach to quantify the factor of safety (FOS) of a
274 point based on the current state of stress and the change in the suction ($u_a - u_w$) caused by
275 rainwater infiltration. The pore water pressure, u_w , can be calculated by the pressure head, H_p ,
276 ($u_w = \rho_w g H_p$, ρ_w is the density of water with the value of 1000 kg/m^3). Afterward, the 3D
277 distribution of soil moisture and related u_w in the saturated and unsaturated zone during a
278 rainfall event is coupled with the 3D soil mechanics model in two ways. One is that the
279 volumetric water content, θ , is applied to the 3D soil mechanics model as body load to manifest
280 the effect of moisture variation on the self-weight and stress distribution as follows.

$$281 \quad \nabla \cdot (\boldsymbol{\sigma}) + \gamma(\theta)\mathbf{b} = 0 \quad (18)$$

282 where, $\boldsymbol{\sigma}$ is the stress tensor (kPa); \mathbf{b} is the unit vector of body forces, and γ is the bulk unit
283 weight (N/m^3), which is a function of the volumetric water content θ .

284 Another is that the negative pore water pressure (suction) in the unsaturated zone will
285 increase the effective stress of the soil, while the positive pore water pressure in the saturated
286 zone due to groundwater will decrease the effective stress of the soil. The influence of the
287 suction on the effective stress is evaluated with Bishop's effective stress ([Bishop, 1954](#)).

$$288 \quad \sigma' = (\sigma - u_a) + \chi(u_a - u_w), \quad \chi = \frac{S_e - S_r}{1 - S_r} \quad (19)$$

289 where, σ' is effective stress (kPa); u_a is the pore air pressure (kPa); u_w is the pore water pressure
290 (kPa), and χ is the matrix suction coefficient which varies from 0 to 1 depending on the degree
291 of saturation. S_r is the residual degree of saturation. Finally, the local factor of safety (F_{LFS}) at
292 each point within a hillslope can be defined as follows.

$$293 \quad F_{LFS} = \frac{2 \cdot \cos \phi'}{\sigma'_1 - \sigma'_3} \left[c' + \frac{\sigma'_1 + \sigma'_3}{2} \tan \phi' \right] \quad (20)$$

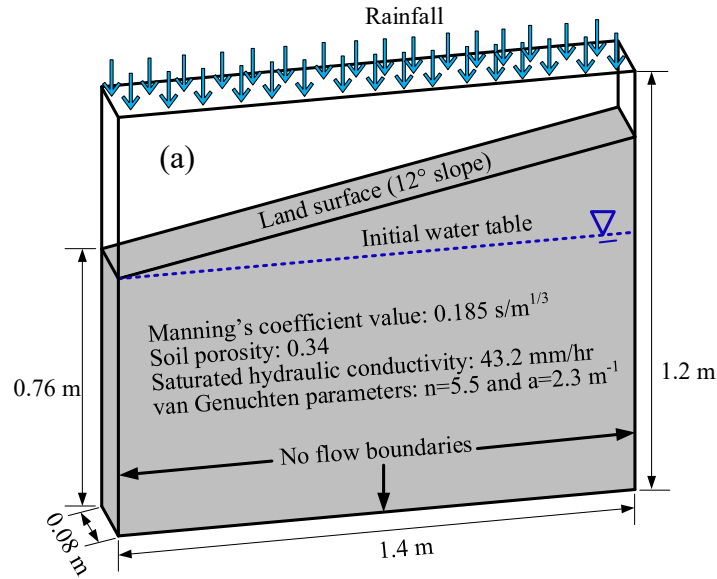
294 where, c' is the effective cohesion (kPa); ϕ' is the effective friction angle ($^{\circ}$); σ_1' and σ_3' are
295 the maximum and minimum principal stress for the unsaturated soil (kPa).

296 **4 Validation of the Iterative Cross-coupled Surface and Subsurface Flows Model**

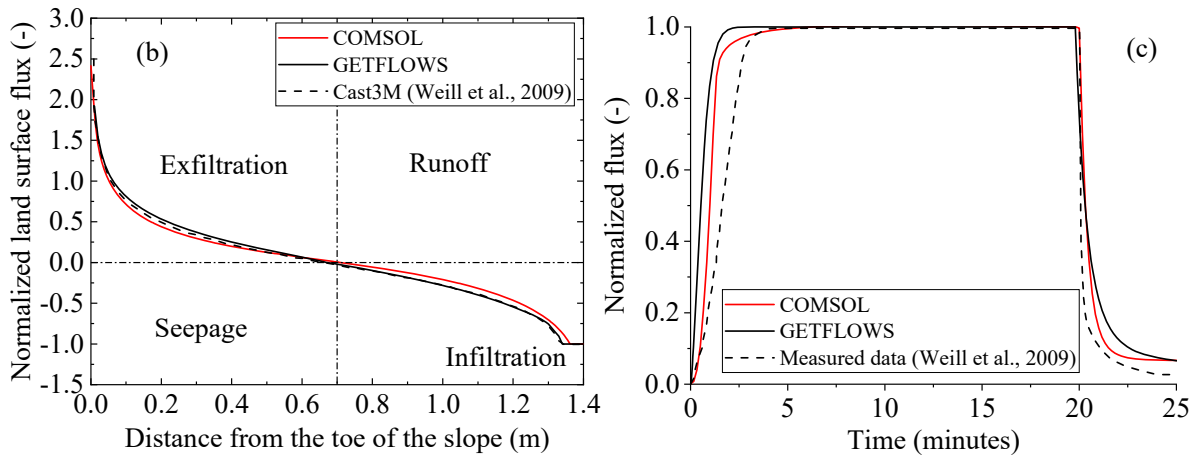
297 In this part, the iterative cross-coupled surface and subsurface flows model proposed in
298 chapter 2 is verified by the experimental system presented by [Abdul and Gillham \(1984\)](#). The
299 experimental system is composed of a 1.4 m×1.2 m×0.08 m Plexiglas box filled with medium-
300 fine sand as illustrated in Fig. 4(a). The free water is drained off at the toe of the slope, and the
301 initial water table is located at the toe of the slope. The soil properties are shown in Fig. 4(a).
302 A rainfall rate of 43.2 mm/hr is applied on the whole surface domain in the first 20 minutes of
303 a total time of 25 minutes. To verify the simulation results of the proposed coupled model, the
304 experimental system is also simulated by a commercial software, GETFLOWS ([GETFLOWS,](#)
305 [2014](#)), which is a finite difference fluid flow numerical simulator. [Kitamura et al. \(2016\)](#) and
306 [Malow et al. \(2017\)](#) validated the applicability of GETFLOWS for simulating the surface flow
307 and subsurface flow process by comparing the simulation results of GETFLOWS and
308 measurements of river water levels in the area of eastern Fukushima Prefecture in Japan and
309 the area of Kourtimalei in Djibouti, respectively. The difference between GETFLOWS and the
310 proposed model in this study in terms of theory and governing equations is that GETFLOWS
311 simulate surface and subsurface flows in a fully coupled way by using air and water two-phase
312 flows, and the governing equation of mass conservation is expressed as follows ([Mori et al.,](#)
313 [2015](#)).

$$314 \quad \frac{\partial(\varphi S_p)}{\partial t} - \nabla \cdot (u_p) = q_p, \quad p = (\text{water, air}) \quad (21)$$

315 where, subscript p indicates fluid phase, water (w) or air (a); φ is the effective porosity (m^3/m^3);
316 S_p is fluid saturation of p phase, ($S_w + S_a = 1$); u_p is the fluid flow velocity of p phase (Pa); q_p is
317 the volumetric flux of sink and source of p phase ($\text{m}^3/\text{m}^3/\text{s}$).



318



319

320

321

322

Fig. 4. (a) Abdul and Gillham system; (b) Comparison of calculated results of normalized flux along the land surface at the 19 minutes after rain; (c) Comparison of calculated results and measured data of normalized flux of discharge at the toe of the slope.

323

324

325

326

327

328

Fig. 4(b) and Fig. 4(c) plot the results calculated by COMSOL and GETFLOWS compared with the results calculated by Cast3M (a finite element code that was used by Weill et al. (2009) for modeling surface/subsurface flow in a fully integrated way, which is similar to GETFLOWS), and measured data referred from Weill et al. (2009). Fig. 4(b) shows the fluxes along the land surface, and all the fluxes are normalized by the rainfall flux imposed at the land surface (entering fluxes are negative by convention). The results imply that the models

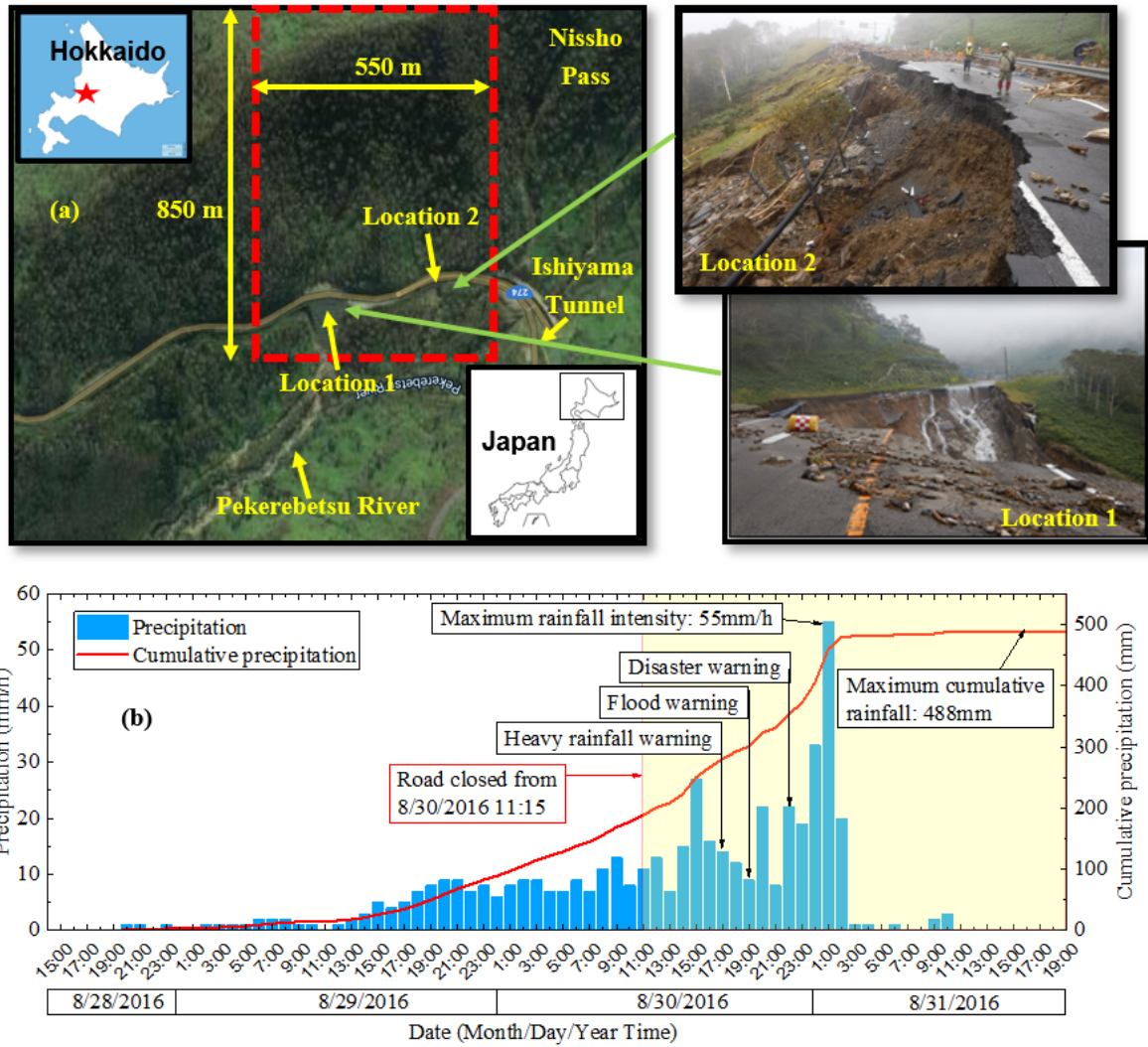
329 implemented in COMSOL and GETFLOWS are able to describe the three surface regimes
330 (infiltration, runoff, and exfiltration) along the land surface: in a small area at the top of the
331 slope, all rainwater infiltrates into the soil (normalized flux equals -1); in the upper half of the
332 slope, part of the rainwater infiltrates, and the rest flows in the form of runoff on the land
333 surface (normalized flux between -1 and 0); at the lower half of the slope, groundwater
334 exfiltrates to the land surface and flows out with the runoff from the upper part (normalized
335 flux positive). Fig. 4(c) displays the normalized flux of discharge at the toe of the slope
336 calculated by COMSOL and GETFLOWS compared with the data measured by [Weill et al.](#)
337 [\(2009\)](#). It shows that the calculated results agree well with the measured data, though the
338 simulated time to reach the steady state of overland water and groundwater exchange is shorter
339 than the experimental one. The presence of air could significantly slow down the infiltration
340 process ([Weill et al., 2009](#)), and the inconsideration of this effect in the modeling approach
341 could be responsible for that.

342 **5 Case Study of Typhoon Induced Embankment Slope Failures**

343 5.1 Outline of disasters

344 In 2016, from the Pacific, Typhoon No.10 (Lionrock) landed on Hokkaido, Japan on
345 August 29th-31st, and the sediments eroded and transported from slopes and banks during the
346 event were estimated to be approximately $3.7 \times 10^5 \text{ m}^3$ within the Pekerebetsu catchment in
347 Hokkaido, Japan ([Furuichi et al., 2018](#)). Near to Nissho Pass along the National Highway Route
348 274 in Hokkaido, Japan, Typhoon No.10 triggered intense landslides, embankment collapses,
349 and debris flows as shown in Fig. 5(a). According to the rainfall records obtained from
350 Automated Meteorological Data Acquisition System (AMeDAS), the observed cumulative
351 rainfall that fell from 19:00 on August 28th to 10:00 on August 31st was 488 mm with the peak
352 value of 55 mm at 01:00 on August 31st as shown in Fig. 5(b), which is the highest rainfall ever

353 recorded in that area. Based on the prediction of the occurrence of sediment-related disasters
 354 by the Japanese early warning system, the road was closed from 11:15 on August 30th, and
 355 Hokkaido government released heavy rainfall warning information, flood warning information,
 356 and disaster warning information at 17:00, 19:00, and 22:00 on August 30th, respectively.

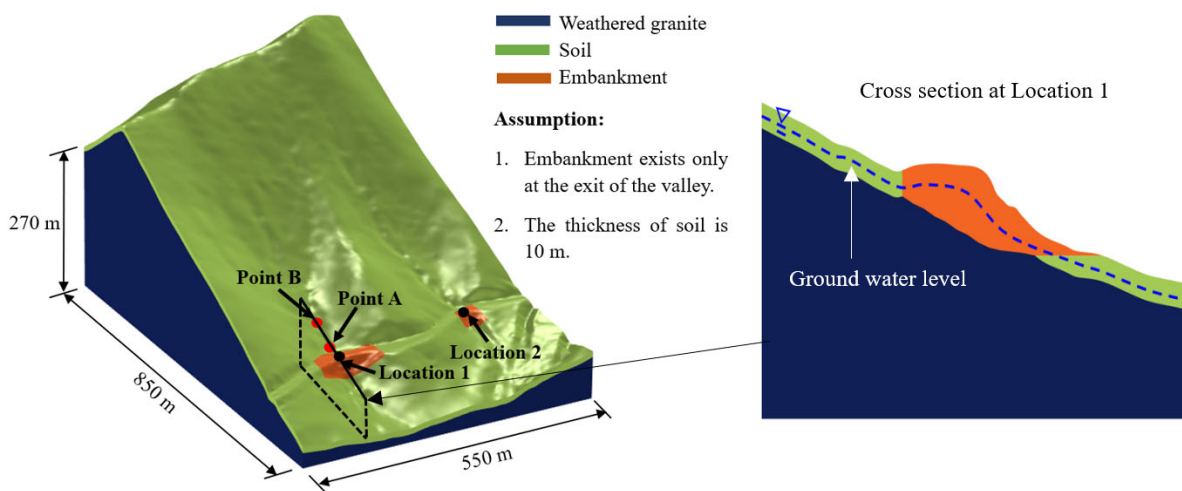


357
 358 **Fig. 5.** (a) Locations of slope failures induced by Typhoon No.10 along National
 359 Highway Route 274; (b) Rainfall recorded during Typhoon No.10 at Nissho Pass.

360 5.2 Simulation of surface and subsurface flows for a natural mountain area

361 The surface flow and subsurface flow analysis at Nissho Pass are performed by the
 362 proposed coupled model. Based on the digital elevation model (DEM) produced from airborne

363 laser scanning (1m resolution), a 3D model for a natural mountain area (surrounded by the red
 364 dashed box in Fig. 5(a)) for slope instabilities assessment with surface and subsurface flows
 365 analysis is built as shown in Fig. 6. The model is composed of three parts: weathered granite,
 366 soil, and embankment. Soil properties are listed in Table 2. The parameters, i.e. dry density
 367 (ρ_s), saturated hydraulic conductivity (k_s), saturated volumetric water content (θ_s), effective
 368 cohesion (c'), and effective friction angle (ϕ'), have been obtained from laboratory element
 369 tests (Sato et al., 2017). The parameters for which no results of laboratory tests are available,
 370 i.e. residual volumetric water content (θ_r) and van Genuchten parameters (α and m), were
 371 estimated based on the grain size curve of soil (SoilVision, 2018). Although there were three
 372 other typhoons before Typhoon No.10, since they were at least one week apart from Typhoon
 373 No.10, they had little effect on the groundwater level during Typhoon No.10. Therefore, the
 374 initial groundwater level is set to -5.5m from the ground surface according to the historical
 375 measured average value in the same period of previous years. Manning's coefficient value is
 376 $0.3 \text{ s/m}^{1/3}$ for the slope, which is the recommended value of Japan Institute of Country-ology
 377 and Engineering (JICE) for mountain grassland. The simulation time is from 19:00 on August
 378 28th, 2016 to 17:00 on August 31st, 2016 for a total of 70 hours with the timestep of 1 hour.



379

380 **Fig. 6.** Three-dimensional numerical model of a natural mountain area at Nissho Pass.

381

Table 2 Soil properties used for the simulation of the natural mountain area.

Parameters	Embankment	Soil	Weathered granite
Dry density, ρ_s (kg/m ³)	1695	1020	2000
Effective cohesion, c' (kPa)	0	0	37
Effective friction angle, ϕ' (°)	37	35	21
Saturated hydraulic conductivity, k_s (m/s)	1.12×10^{-5}	1.4×10^{-6}	3.47×10^{-9}
Saturated volumetric water content, θ_s (m ³ /m ³)	0.36	0.63	0.48
Residual volumetric water content, θ_r (m ³ /m ³)	0.035	0.19	0.008
van Genuchten parameter, α (1/m)	0.538	0.810	0.012
van Genuchten parameter, m	0.468	0.437	0.246

382

As there are no measurement data at the locations where the slope failures occurred,

383

the simulated results in this study are theoretically verified by a physical runoff model (Tank

384

model) proposed by [Sugawara et al. \(1974\)](#), which uses multi-layered tanks to simulate

385

rainwater infiltration and surface runoff. The Tank model has been proved that it is effective

386

for describing the outflow in the watershed ([Hong et al., 2015](#)). The calculation of runoff is

387

based on the generic value of the parameters suggested by [Okada \(2001\)](#) as listed in Fig. 7. The

388

water storage depth (mm) for each tank is calculated based on the equations below.

389

$$\frac{dH_1}{dt} = R - I_1 - q_{11} - q_{12} \quad (22)$$

390

$$\frac{dH_2}{dt} = I_1 - q_2 - I_2 \quad (23)$$

391

$$\frac{dH_3}{dt} = I_2 - q_3 - I_3 \quad (24)$$

392

The outflow rate from each outlet of the model and infiltration rate from the upper tank

393

to the lower tank is calculated based on the equations below.

394

$$q_{11} = \begin{cases} \alpha_{11} \times (H_1 - L_{11}) & , \text{if } H_1 > L_{11} \\ 0 & , \text{if } H_1 \leq L_{11} \end{cases} \quad (25)$$

395
$$q_{12} = \begin{cases} \alpha_{12} \times (H_1 - L_{12}) & , \text{if } H_1 > L_{12} \\ 0 & , \text{if } H_1 \leq L_{12} \end{cases} \quad (26)$$

396
$$q_2 = \begin{cases} \alpha_2 \times (H_2 - L_2) & , \text{if } H_2 > L_2 \\ 0 & , \text{if } H_2 \leq L_2 \end{cases} \quad (27)$$

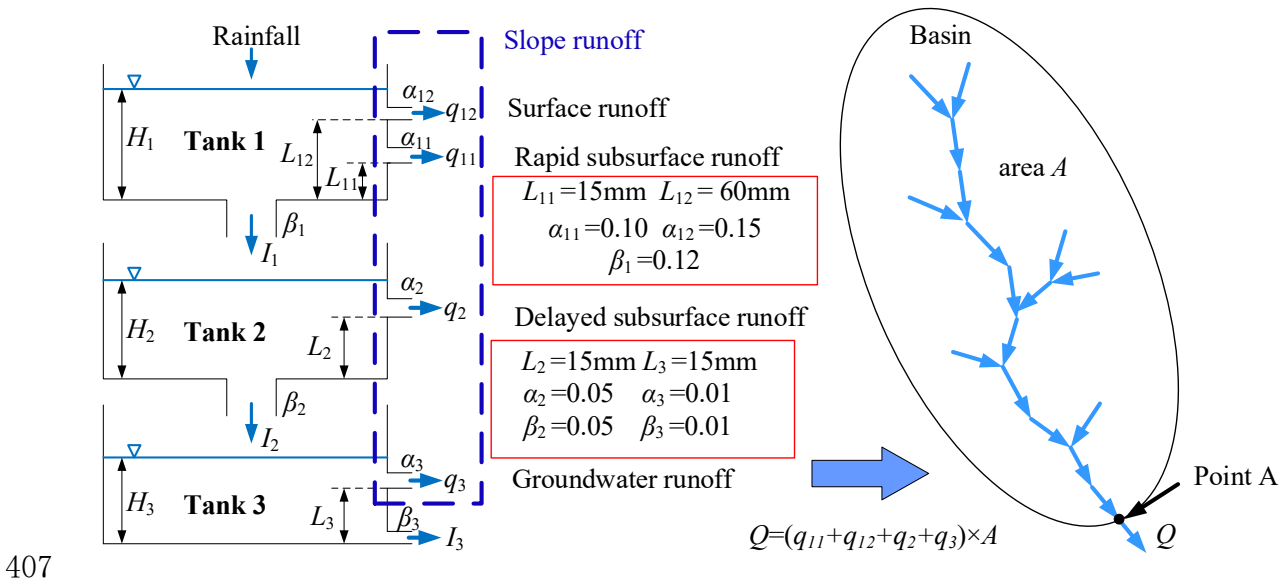
397
$$q_3 = \begin{cases} \alpha_3 \times (H_3 - L_3) & , \text{if } H_3 > L_3 \\ 0 & , \text{if } H_3 \leq L_3 \end{cases} \quad (28)$$

398
$$I_1 = \beta_1 \times H_1, \quad I_2 = \beta_2 \times H_2, \quad I_3 = \beta_3 \times H_3 \quad (29)$$

399 The total outflow rate of the basin is represented as follows.

400
$$Q = (q_{11} + q_{12} + q_2 + q_3) \times A \quad (30)$$

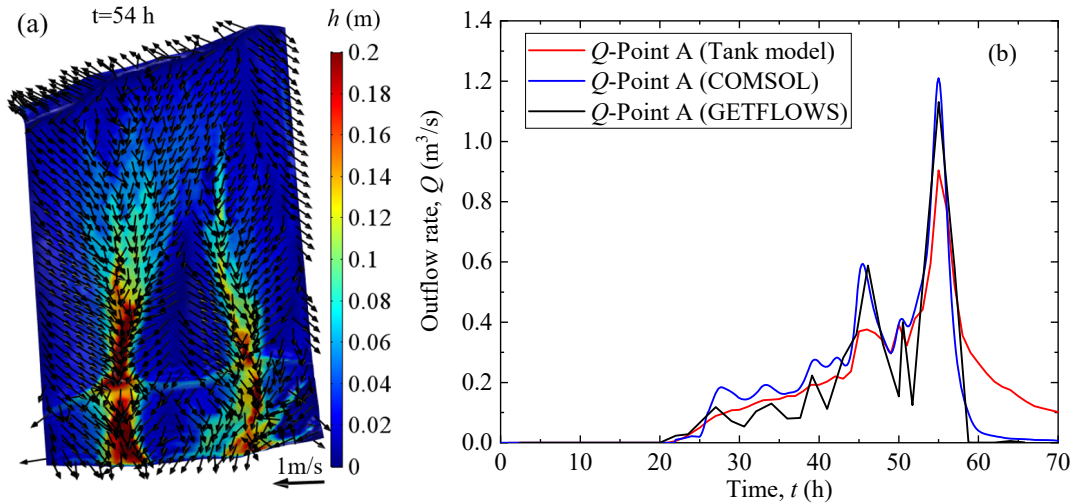
401 where, I_1 , I_2 , and I_3 are the infiltration rate from the upper tank to the lower tank (mm/h); q_{11} ,
 402 q_{12} , q_2 , and q_3 are the outflow rate (mm/h) for each outlet of sidewall; L_{11} , L_{12} , L_2 , and L_3
 403 represent each outlet height (mm); H_1 , H_2 , and H_3 are the water storage depth (mm) in each
 404 layer; α_{11} , α_{12} , α_2 , and α_3 are the outflow coefficient (1/h) for each outlet; β_1 , β_2 , and β_3 are the
 405 coefficients of permeability (1/h) from the bottom hole of each tank; Q is total of outflow rate
 406 of the basin (m^3/s), and A is the area of the basin (km^2).



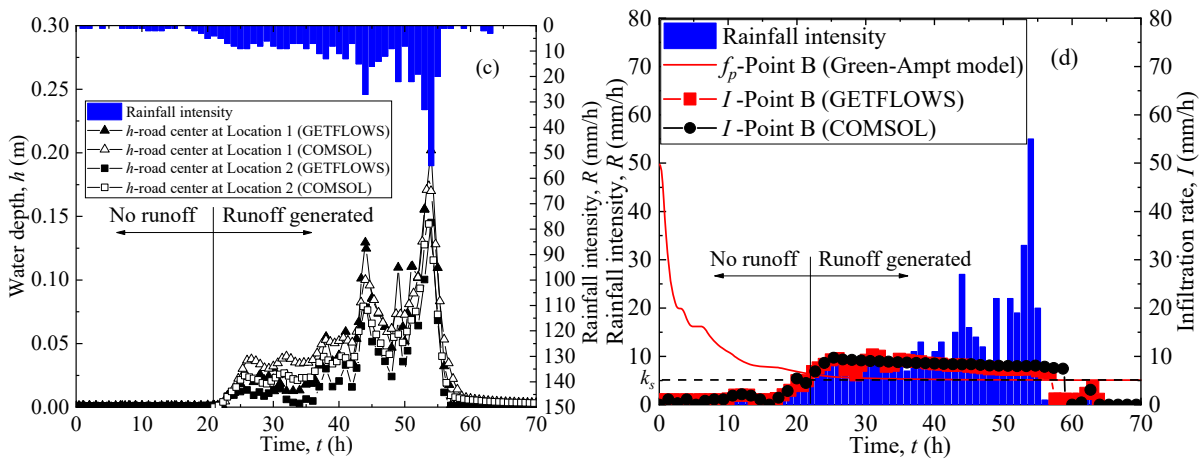
408 **Fig. 7.** Schematic diagram of the three-layer Tank model.

409 Fig. 8(a) displays the distribution of water depth and the vector of flow velocity
410 calculated by COMSOL. From Fig. 8(a), it can be seen that a large amount of water from the
411 upstream is gathered at Location 1 and Location 2, which allows more water to infiltrate into
412 the embankment. The outflow rates of the catchment area at Location 1 (Point A in Fig. 6 and
413 Fig. 7) calculated by the Tank model, COMSOL, and GETFLOWS are shown in Fig. 8(b). To
414 avoid the calculation errors caused by the water coming from Location 2 along the road (see
415 Fig. 5(a) and Fig. 8(a)), Point A is located on the edge of the embankment on the side of the
416 mountain. From Fig. 8(b), it is recognized that the outflow rates calculated by the Tank model,
417 COMSOL, and GETFLOWS are quite similar suggesting that the numerical results are reliable.
418 Tank model assumes that the slope runoff flows out of the catchment area according to a certain
419 percentage of water storage depth in each tank. Accordingly, the Tank model does not consider
420 the impact of slope angle, which causes the outflow rate calculated by the Tank model is
421 smaller at the peak value, and larger at the end of the rainfall event than that calculated by
422 COMSOL and GETFLOWS. Fig. 8(c) plots the surface water depth located at the road center
423 (where water comes from the upstream catchment and road) at Location 1 and Location 2. To
424 discuss the two-stage process of rainwater infiltration, a representative point on the hillside
425 slope (Point B in Fig. 6, located in the gully upstream of Location 1) is selected to display the
426 relationship between infiltration rate and rainfall intensity on the hillside slope as shown in Fig.
427 8(d). The results shown in Fig. 8(d) suggest that at the beginning of a rainfall event, the
428 infiltration rate is equal to the rainfall intensity (all rainwater infiltrates into the soil). From Fig.
429 8(c), it is recognized that the runoff simulated by COMSOL and GETFLOWS is generated
430 from 22 hours after the rainfall event happens, which is consistent with the results calculated
431 by the Tank model shown in Fig. 8(b). Nearly at the same time, rainfall intensity exceeds the
432 infiltration capacity (f_p) of the ground surface in Fig. 8(d).

433



434



435

Fig. 8. (a) Distribution of water depth and the vector of flow velocity calculated by

436

COMSOL; (b) Comparison of outflow rate (Q) calculated by each approach; (c) Surface

437

water depth (h) at Location 1 and Location 2; (d) Infiltration capacity (f_p) and infiltration rate

438

(I).

439

After rainfall intensity exceeds the infiltration capacity (f_p), i.e. the runoff is generated,

440

the infiltration rate is no longer equal to rainfall intensity. At this time, the infiltration rate is

441

governed by the pressure head gradient. The pressure head gradient is controlled by the water

442

depth and the pressure head in the cell below. With the rainwater infiltration, the increase of

443

the pressure head in the cell below is more significant than the increase of the water depth. It

444

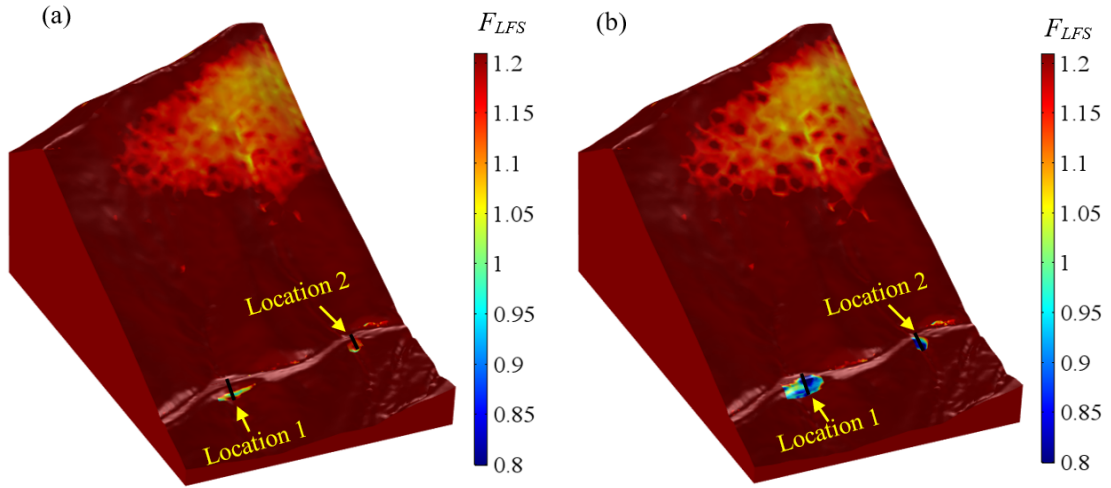
means that the pressure head gradient will become smaller compared with when the runoff is

445 just generated, i.e., the infiltration rate decreases with time during runoff as shown in Fig. 8(d).
446 Furthermore, the surface water depth (Fig. 8(c)) and infiltration rate (Fig. 8(d)) calculated by
447 GETFLOWS agree well with the results calculated by COMSOL at both Location 1 and
448 Location 2, meaning that the two software can be mutually verified and the coupled surface
449 and subsurface flows model is more reliable than Tank model.

450 5.3 Slope instabilities assessment along the highway on a small catchment-scale

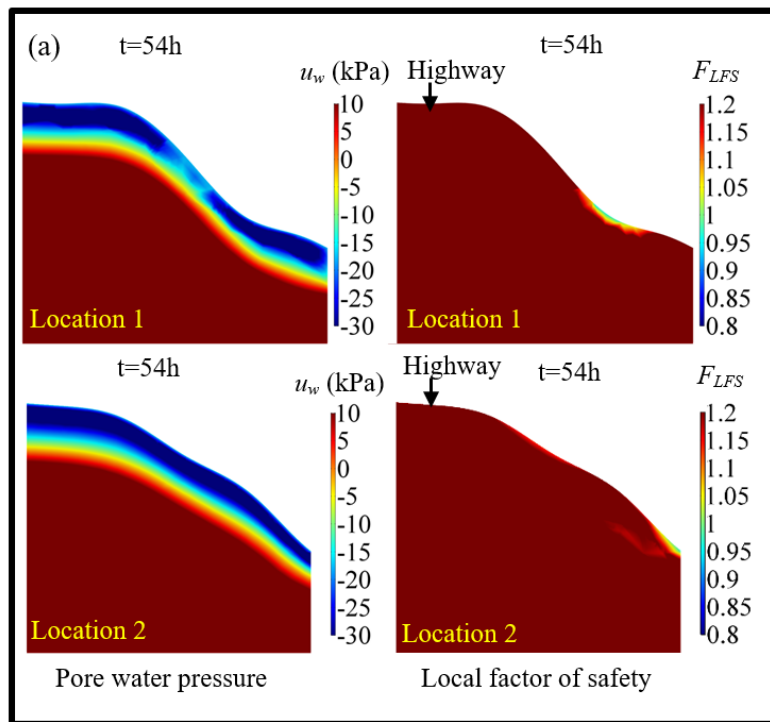
451 In order to investigate the effect of runoff and subsurface flow on the slope stability
452 during Typhoon No.10, the slope instabilities on a small catchment-scale (including two
453 embankment slopes at Location 1 and Location 2, respectively) are analyzed by using the
454 proposed coupled model. The effects of runoff on the infiltration and subsurface flow are
455 considered by the coupled surface and subsurface flows model proposed in chapter 2. By
456 incorporating the body load (volumetric water content) and pore water pressure (u_w) calculated
457 by the coupled surface and subsurface flows model into the soil mechanics model, two cases
458 are studied, i.e., slope instabilities analysis with considering runoff and without. Fig. 9 shows
459 the distribution of the local factor of safety (F_{LFS}) in the two cases. From Fig. 9(b), it is
460 recognized that with considering runoff, the safe area and two dangerous spots are identified
461 in a 550m wide and 850m long area during the heavy rainfall, i.e., the slope failure occurred
462 ($F_{LFS} < 1.0$) at Location 1 and Location 2 are successfully reproduced. Conversely, without
463 considering runoff, slope failure only occurred in a very small area at Location 1 as shown in
464 Fig. 9(a). Fig. 10 shows the distributed pore water pressure (u_w) and local factor of safety (F_{LFS})
465 at Location 1 and Location 2 under the two study cases (with considering runoff and without).
466 From Fig. 10, it can be seen that the presence of runoff leads to a more significant increase in
467 pore water pressure. The negative pore water pressure increases to zero or even becomes
468 positive pore water pressure in the surface layer of the soil, which causes the occurrence of the

469 slope failure. From Fig. 10(b), it can be seen that the simulated slip surface (red line in Fig.
470 10(b)) is slightly shallower than the actual slip surface (blue line in Fig. 10(b)) at Location 2.
471 The main reason why the simulated slip surface is slightly shallower than the actual slip surface
472 is that in the actual process of slope failure, the collapsed part moved downstream, and runoff
473 further eroded the newly exposed soil and caused further damage of the embankment.
474 Therefore, it implies that runoff has significant effects on the embankment slope failures
475 especially at the exit of the gully. On the other hand, by using the LFS approach, slope
476 instabilities analysis can be performed on a small catchment-scale, which has significant
477 advantages as compared with other methods to analyze the stability of a single slope. Moreover,
478 the distribution map of FOS conduces to determine the dangerous spots in the target area. This
479 has significant implications for precisely determining the dangerous spots (instead of areas) on
480 a small catchment-scale and accurately releasing warning information to the dangerous spots.
481 For example, in Japan, the disaster warning information is released to a 5 km×5 km area
482 according to the national early warning system. Based on the early warning system, the
483 occurrence time of slope failures can be roughly estimated, while it is difficult to determine the
484 specific number and location of slope failures. Therefore, the coupled model of surface flow,
485 subsurface flow, and soil mechanics proposed in this study provides an effective way for
486 simulating heavy rainfall-induced runoff and slope instabilities in the target area. By expanding
487 the size of the coupled model proposed in this paper to 5 km×5 km, the occurrence of slope
488 failures can be roughly predicted by the Japan early warning system, and the dangerous spots
489 can be identified in this wide area by the numerical results. It means that combining the
490 numerical simulation results with the prediction results of an early warning system, warning
491 information will be accurately released to the dangerous spots instead of broader areas.

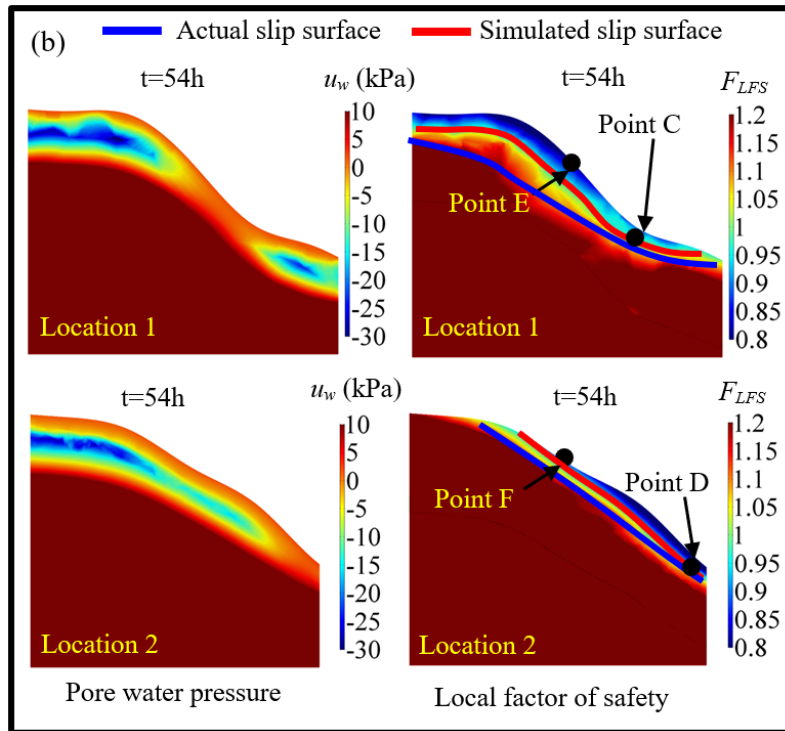


492
493
494

Fig. 9. Distribution map of FOS on the small catchment-scale during Typhoon No.10. (a) Without considering runoff; (b) With considering runoff.



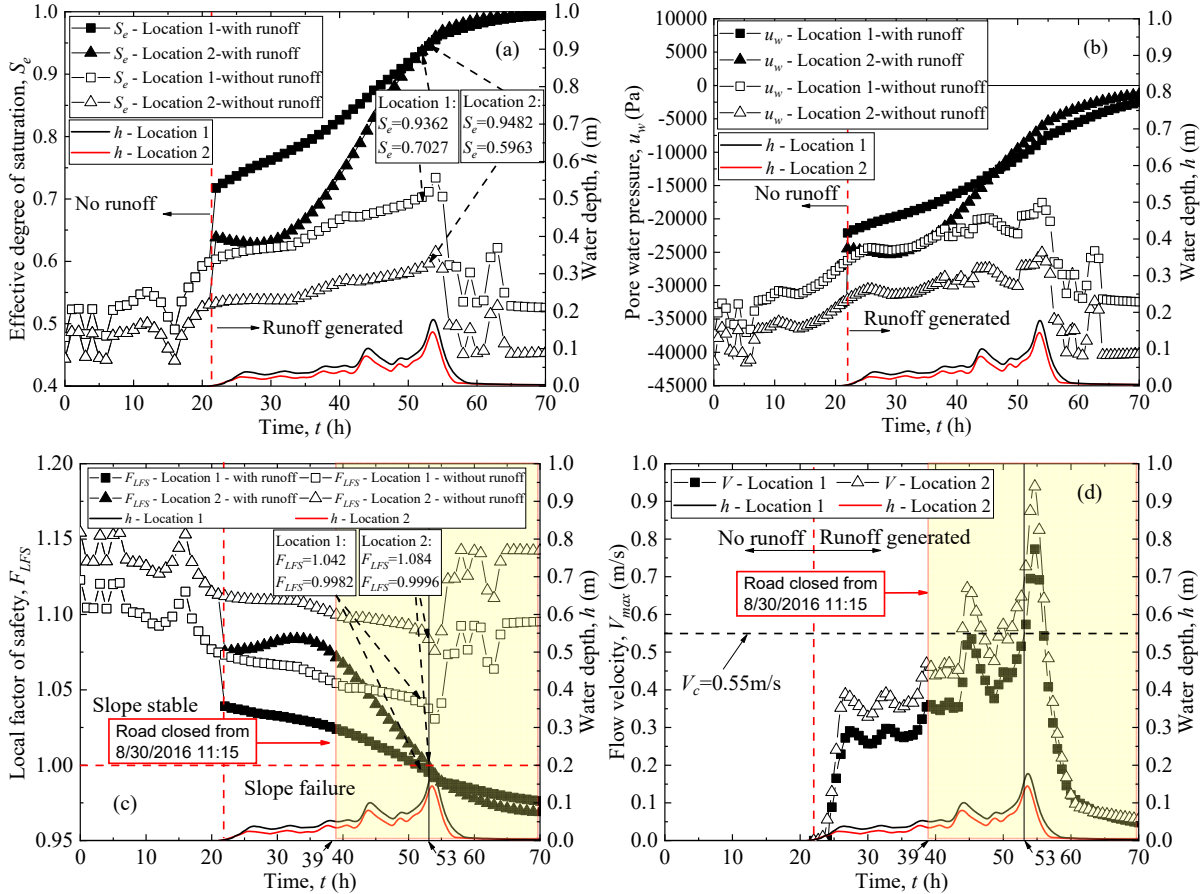
495



496
 497 **Fig. 10.** Distribution of pore water pressure (u_w) and local factor of safety (F_{LFS}). (a)
 498 Without considering runoff; (b) With considering runoff.

499 To further analyze the effect of runoff on slope stability, Fig. 11(a) to Fig. 11(c)
 500 illustrates the time-dependent effective degree of saturation (S_e), u_w , and F_{LFS} at Location 1 and
 501 Location 2 (Point C and Point D in Fig. 10, located near the ultimate slip surface as shown by
 502 the red lines in Fig. 10(b)). It is recognized that the infiltrated rainwater causes the increase of
 503 the S_e as shown in Fig. 11(a), which causes an increase in the u_w as shown in Fig. 11(b), thereby
 504 causing a decrease in the suction of unsaturated soil, and eventually decreases the F_{LFS} as shown
 505 in Fig. 11(c). It is worth noting that the increase of S_e and u_w , and the decrease of F_{LFS} are more
 506 significant when the runoff is considered. After runoff is generated, S_e and u_w have a steep
 507 increase and F_{LFS} sharp declines, meaning that the runoff from upstream allows more water to
 508 infiltrate into the embankment, thereby causing a more significant decrease in the suction of
 509 the embankment and the possibility of embankment slope failure at the exit of the gully to be
 510 much greater than other locations along the highway. On the other hand, the excessive high-

511 velocity runoff could allow more water to infiltrate into the embankment and eventually trigger
512 slope failure. Therefore, the runoff is a key factor causing the embankment slope failures, and
513 its effects cannot be neglected. Erosion might occur on the slope surface when the flow velocity
514 exceeds a critical value, called critical erosional velocity, V_c (Blais and McGinn, 2011). The
515 critical erosional velocity is 0.55m/s at Location 1 and Location 2, which is calculated by the
516 critical erosion velocity estimation model ($V_c=0.33D_{50}^{0.47}$) proposed by Bogardi (1978). V_c is
517 critical erosion velocity measured in m/s. D_{50} represents the median diameter of the sediment
518 material in mm, and its value is 3.0 mm for the embankment at Nissho Pass (Kawamura and
519 Miura, 2018). To discuss the effects of the runoff on the erosion of the embankment slope
520 surface, Fig. 11(d) shows the flow velocity (V) on the embankment slope at Location 1 and
521 Location 2 (Point E and Point F in Fig. 9, located on the embankment slope surface). In Fig.
522 11(d), it can be identified that the flow velocity exceeds the critical erosion velocity, V_c (0.55
523 m/s), and even close to 1.0 m/s at peak both at Location 1 and Location 2. Therefore, it can be
524 considered as the excessive high-velocity runoff and could cause severe erosion of the
525 embankment slope. Moreover, from Fig. 11(c) and Fig. 11(d), it is recognized that the F_{LFS}
526 becomes less than 1.0 and the flow velocity exceeds V_c at 00:00 on August 31st, 2016 after the
527 road was closed from 11:15 on August 30th, 2016 (the yellow period in Fig. 11(c) and Fig.
528 11(d)). It means that the simulation results are reliable. However, the runoff induced erosion
529 of the embankment slope is not considered in the numerical simulation of this study. The
530 discussion in the effects of runoff on the erosion of the embankment slope surface and the
531 influences of the erosion on the slope instability is a future assignment in this study.



532

533

534

535

536

537

6 Discussions and Conclusions

538

539

540

541

542

543

544

Fig. 11. Time-dependent effective degree of saturation (S_e), pore water pressure (u_w), local factor of safety (F_{LFS}), and flow velocity (V) at Location 1 and Location 2. (a) S_e vs. time; (b) u_w vs. time; (c) F_{LFS} vs. time; (d) V vs. time.

545 the general commercial software used for stability analysis of slopes can hardly simulate runoff,
546 for example, GeoStudio and FLAC^{3D}. Ignoring runoff is still the main calculation assumptions
547 of surface hydrology in these software. Therefore, this study proposes a coupled model of
548 surface flow, subsurface flow, and soil mechanics, which provides an effective way for
549 simulating heavy rainfall-induced runoff and slope instabilities on a small catchment-scale. In
550 addition, combining the numerical simulation results of the coupled model proposed in this
551 paper with the prediction results of the Japanese early warning system in the target area (e.g. 5
552 km×5 km), warning information will be accurately released to the dangerous spots instead of
553 areas. The findings from this study can be outlined as follows:

554 1. In the equations of motion of shallow water equations, the driving force term and friction
555 term are the main contribution terms, while the total contribution of the inertia term, advection
556 term, and velocity term is less than 1% together. Therefore, the diffusion wave approximation
557 that simplifies the equations of motion by considering only the driving force term and friction
558 term is applicable to the practical runoff analysis.

559 2. The coupled model of surface flow, subsurface flow, and soil mechanics proposed in this
560 study can reflect the two-stage process of rainwater infiltration, i.e. rainfall infiltration in the
561 early stage of rainfall event and runoff infiltration in the later stage of the rainfall event, and it
562 is also applicable to simulate runoff, infiltration, seepage, and slope instabilities on a small
563 catchment-scale.

564 3. Excessive high-velocity runoff is a key factor causing the embankment slope failures at the
565 exit of the gully, and its effects cannot be neglected. In this study, runoff and slope stability
566 with two watersheds (each including an embankment slope) are successfully simulated by the
567 coupled model of surface flow, subsurface flow, and soil mechanics proposed in this study.

568 The effects of runoff on the slope stability are successfully taken into consideration and the
569 slope failures caused by runoff are reproduced through numerical simulation.

570 4. The LFS approach is more efficient to predict the rainfall-induced slope failures in the target
571 area by simulating slope instabilities on a small catchment-scale, which has significant
572 advantages as compared with other methods to analyze the stability of a single slope.
573 Furthermore, the distribution map of FOS on the small catchment-scale conduces to determine
574 the dangerous spots in the target area.

575 The research findings of this study are expected to help improve the numerical model
576 of heavy rainfall-induced surface flow and slope failure, and benefit the prediction of the
577 occurrence of heavy rainfall-induced disasters in the future. Expanding the coupled model
578 proposed in this study to a larger area with more watersheds and combining the numerical
579 results with the prediction results of the Japanese early warning system, as well as the
580 discussion in the effects of runoff on the erosion of the embankment slope surface and the
581 influences of the erosion on the slope instability are future assignments in this study.

582 **Acknowledgments**

583 This study was supported in part by Grants-in-Aid for Scientific Research (A) (16H02360)
584 from the Japan Society for the Promotion of Science (JSPS) KAKENHI. The authors gratefully
585 acknowledge the Hokkaido Regional Development Bureau and Hokkaido Road Management
586 Engineering Center for their surveyed data and comments.

587 **Data Availability**

588 Weather station data and terrain information used in this research are publicly available at the
589 website of Japan Meteorological Agency (<http://www.data.jma.go.jp/gmd/risk/obsdl/index.php>)
590 and Geospatial Information Authority of Japan (<https://www.gsi.go.jp/top.html>). The results

591 data obtained in this research are available at the website
592 (<https://data.mendeley.com/datasets/2n9zyyyfyz/1>).

593 **References**

594 Abdul, A. S., Gillham, R. W., 1984. Laboratory studies of the effects of the capillary fringe on
595 streamflow generation. *Water Resources Research*. 20 (6), 691-698. doi:
596 10.1029/WR020i006p00691

597 Acharya, G., Cochrane, T. A., Davies, T., Bowman, E., 2009. The influence of shallow
598 landslides on sediment supply: a flume-based investigation using sandy soil. *Engineering*
599 *Geology*. 109(3-4): 161-169. doi.org/10.1016/j.enggeo.2009.06.008

600 Bishop, A. W., 1954. The use of pore water coefficients in practice, *Géotechnique*. 4, 148-152.
601 doi:10.1680/geot.1954.4.4.148

602 Bishop, A. W., 1955. The use of slip circle in the stability analysis of slopes. *Géotechnique*.
603 5(1), 7-17. doi:10.1680/geot.1955.5.1.7

604 Blais, E. L., McGinn, R. A., 2011. Critical erosion velocity for natural shale gravels: an
605 empirical study. *Prairie Perspectives: Geographical Essays*. 14, 51-59.

606 Bogardi, J., 1978. *Sediment Transport in Alluvial Streams* (No. 04; TC175. 2, B6.). Budapest:
607 Akademiai Kiado, 826 p.

608 Chiu, Y. Y., Chen, H. E., Yeh, K. C., 2019. Investigation of the influence of rainfall runoff on
609 shallow landslides in unsaturated soil using a mathematical model. *Water*, 11(6), 1178.
610 doi: 10.3390/w11061178

611 Chowdhury, R., Flentje, P., 2002. Uncertainties in rainfall-induced landslide hazard. *Quarterly*
612 *Journal of Engineering Geology and Hydrogeology*. 35(1), 61-70. doi:
613 10.1144/qjegh.35.1.61

614 COMSOL Multiphysics, 2018. version 5.4, COMSOL Inc., Sweden.

615 Cuomo, S., Della Sala, M., 2013. Rainfall-induced infiltration, runoff and failure in steep
616 unsaturated shallow soil deposits. *Engineering Geology*. 162, 118-127.
617 doi.org/10.1016/j.enggeo.2013.05.010

618 Farshidfar, N., Nayeri, A., 2015. Slope Stability Analysis by Shear Strength Reduction Method.
619 *Journal of Civil Engineering and Urbanism*. 5(1), 35-37.

620 Fernández-Pato, J., Caviedes-Voullième, D., Garcia-Navarro, P., 2016. Rainfall/runoff
621 simulation with 2D full shallow water equations: Sensitivity analysis and calibration of
622 infiltration parameters. *Journal of Hydrology*. 536, 496-513.
623 doi:10.1016/j.jhydrol.2016.03.021

624 Fujisawa, K., Marcato, G., Nomura, Y., Pasuto, A., 2010. Management of a typhoon-induced
625 landslide in Otomura (Japan). *Geomorphology*. 124(3-4), 150-156. doi:
626 10.1016/j.geomorph.2010.09.027

627 Furuichi, T., Osanai, N., Hayashi, S., Izumi, N., Kyuka, T., Shiono, Y., Miyazaki, T.,
628 Hayakawa, T., Nagano, N., Matsuoka, N., 2018. Disastrous sediment discharge due to
629 typhoon-induced heavy rainfall over fossil periglacial catchments in western Tokachi,
630 Hokkaido, northern Japan. *Landslides*. 15, 1645-1655. doi:10.1007/s10346-018-1005-1

631 GEO-SLOPE International (2007), GeoStudio, Calgary, Alberta, Canada.

632 GETFLOWS, 2014. Integrated Water Cycle Simulation System. Geosphere Environmental
633 Technology Corp., Japan.

634 Green, W. H., Ampt, G. A., 1911. Studies on Soil Physics, Part 1, the Flow of Air and Water
635 through Soils. *Journal of Agricultural Science*. 4(1), 1-24. doi:
636 10.1017/S0021859600001441

637 Hong, N., Hama, T., Kitajima, T., Aqili, S. W., Huang, X., Wei, Q., Kawagoshi, Y., 2015.
638 Simulation of Groundwater Levels Using Tank Model with Consideration of Mixed

639 Hydrological Structure in Kumamoto City. *Journal of Water and Environment*
640 *Technology*. 13(4), 313-324. doi: 10.2965/jwet.2015.313

641 Horton, R. E., 1933. The role of infiltration in the hydrological cycle. *Eos Trans. AGU*. 14,
642 446-460. doi: 10.1029/TR014i001p00446

643 Itasca, 2012. *Fast Lagrangian Analysis of Continua in 3 Dimensions (FLAC3D)*, USA

644 Kawamura, S., Miura, S., 2018. Mechanical behavior of decomposed granite soils in Hokkaido
645 and its evaluation. *Japanese Geotechnical Journal*. 13(2), 159-170. (in Japanese)

646 Kean, J.W., McCoy, S.W., Tucker, G.E., Staley, D.M., Coe, J.A., 2013. Runoff-generated
647 debris flows: Observations and modeling of surge initiation, magnitude, and frequency. *J.*
648 *Geophys. Res. Earth Surf*. 118, 2190-2207. doi: 10.1002/jgrf.20148

649 Kitamura, A., Kurikami, H., Sakuma, K., Malins, A., Okumura, M., Machida, M., Mori, K.,
650 Tada, K., Tawara, Y., Kobayashi, T., Yoshida, T., Tosaka, H., 2016. Redistribution and
651 export of contaminated sediment within eastern Fukushima Prefecture due to typhoon
652 flooding. *Earth Surf. Process. Landforms*. 41, 1708-1726. doi: 10.1002/esp.3944.

653 Liu, J., Yang, C., Gan, J., Liu, Y., Wei, L., Xie, Q., 2017. Stability analysis of road embankment
654 slope subjected to rainfall considering runoff-unsaturated seepage and unsaturated fluid–
655 solid coupling. *International Journal of Civil Engineering*. 15(6), 865-876. doi:
656 10.1007/s40999-017-0194-7

657 Lu, N., Şener-Kaya, B., Wayllace, A., Godt, J. W., 2012. Analysis of rainfall-induced slope
658 instability using a field of local factor of safety. *Water Resources Research*. 48, W09524.
659 doi:10.1029/2012WR011830

660 Malow F.A., Shimada S., Hazart A., 2017. Event-based Rainfall-runoff Simulations using
661 GETFLOWS for Kourtimalei Catchment in Djibouti. *International Journal of*
662 *Environmental and Rural Development*. 8 (1), 169-175.

663 Morgenstern, N. R., Price V. E., 1965. The analysis of the stability of general slip surfaces.
664 Géotechnique. 15(1), 79-93. doi: 10.1680/geot.1965.15.1.79

665 Mori, K., Tada, K., Tawara, Y., Ohno, K., Asami, M., Kosaka, K., Tosaka, H., 2015. Integrated
666 watershed modeling for simulation of spatiotemporal redistribution of post-fallout
667 radionuclides: Application in radiocesium fate and transport processes derived from the
668 Fukushima accidents. *Environmental Modelling & Software*. 72, 126-146. doi:
669 10.1016/j.envsoft.2015.06.012

670 Murillo, J., García-Navarro, P., Burguete, J., Brufau, P., 2007. The influence of source terms
671 on stability, accuracy and conservation in two-dimensional shallow flow simulation using
672 triangular finite volumes. *Int. J. Numer. Methods Fluids*. 54, 543-590. doi:
673 10.1002/fld.1417

674 Okada, K., 2001. Soil Water Index. *Meteorological Society of Japan*, 48(5), 59-66. (in Japanese)

675 Osanai, N., Shimizu, T., Kuramoto, K., Kojima, S., Noro, T., 2010. Japanese early-warning for
676 debris flows and slope failures using rainfall indices with Radial Basis Function Network.
677 *Landslides*. 7, 325-338. doi: 10.1007/s10346-010-0229-5

678 Pasculli, A., Calista, M., Sciarra, N., 2018. Variability of local stress states resulting from the
679 application of Monte Carlo and finite difference methods to the stability study of a
680 selected slope. *Engineering Geology*. 245, 370-389. doi:10.1016/j.enggeo.2018.09.009

681 Rahardjo, H., Lee, T. T., Leong, E. C., Rezaur, R. B., 2005. Response of a residual soil slope
682 to rainfall. *Canadian Geotechnical Journal*. 42(2), 340-351. doi.org/10.1139/t04-101

683 Rengers, F. K., McGuire, L. A., Kean, J. W., Staley, D. M., Hobley, D. E. J., 2016. Model
684 simulations of flood and debris flow timing in steep catchments after wildfire. *Water
685 Resources Research*. 52(8), 6041-6061. doi: 10.1002/2015WR018176

686 Richards, L. A., 1931. Capillary conduction of liquids through porous mediums. *Physics*. 1(5),
687 318-333. doi: 10.1063/1.1745010

688 Sato, A., Hayashi, T., Hayashi, H., Yamaki, M., 2017. On the geotechnical properties of
689 decomposed granite soil in Hokkaido. 57th Technical Report of Hokkaido Branch of
690 Japanese Geotechnical Society. 145-148. (in Japanese)

691 Sciarra, N., Calista, M., Miccadei, E., Pasculli, A., Piacentini, T., Sciarra, M., 2017.
692 Morphometric analysis, multitemporal geomorphological investigation and numerical
693 modelling of the Montebello sul Sangro Large Landslide (Abruzzo-Central Italy). Italian
694 Journal of Engineering Geology and Environment. 1(1), 117-133.
695 doi:10.4408/IJEGE.2017- 01.S-11

696 SoilVision, 2018. Version, 4.23. SoilVision Systems Ltd. Saskatoon, Saskatchewan, Canada.

697 Sugawara, M., Ozaki, E., Watanabe, I., Katsuyama, Y., 1974. Tank model and its application
698 to Bird Creek, Wollombi Brook, Bikin River, Kitsu River, Sanaga River, and Nam Mune.
699 Research Note of the National Research Center for Disaster Prevention 11, Tsukuba,
700 Japan. 1-64.

701 Tian, D., Liu, D., 2011. A new integrated surface and subsurface flows model and its
702 verification. Applied Mathematical Modelling. 35(7), 3574-3586.
703 doi:10.1016/j.apm.2011.01.035

704 van Asch, T.W.J., Yu, B., Hu, W., 2018. The Development of a 1-D Integrated Hydro-
705 Mechanical Model Based on Flume Tests to Unravel Different Hydrological Triggering
706 Processes of Debris Flows. Water, 10(7), 950. Doi:10.3390/w10070950

707 van Genuchten, M. Th., 1980. A closed-form equation for predicting the hydraulic conductivity
708 of unsaturated soils. Soil Science Society of America Journal. 44(5), 892-898. doi:
709 10.2136/sssaj1980.03615995004400050002x

710 Wang, G., Sassa, K., 2003. Pore-pressure generation and movement of rainfall-induced
711 landslides: effects of grain size and fine-particle content. Engineering Geology. 69(1-2),
712 109-125. doi: 10.1016/S0013-7952(02)00268-5

- 713 Wei, Z., Shang, Y., Zhao, Y., Pan, P., Jiang, Y. 2017. Rainfall threshold for initiation of
714 channelized debris flows in a small catchment based on in-site measurement. *Engineering*
715 *Geology*. 217, 23-34. doi.org/10.1016/j.enggeo.2020.105618
- 716 Weill, S., Mouche, E., Patin, J., 2009. A generalized Richards equation for surface/subsurface
717 flow modelling. *Journal of Hydrology*. 366, 9-20. doi: 10.1016/j.jhydrol.2008.12.007
- 718 Zeng, Y. H., Guymer, I., Spence, K. J., Huai, W. X., 2010. Application of analytical solutions
719 in trapezoidal compound channel flow. *River Research and Applications*. 28 (1), 53-61.
720 doi: 10.1002/rra.1433
- 721 Zhang, J., Huang, H. W., Zhang, L. M., Zhu, H. H., Shi, B., 2014. Probabilistic prediction of
722 rainfall-induced slope failure using a mechanics-based model. *Engineering Geology*. 168,
723 129-140. doi.org/10.1016/j.enggeo.2013.11.005